Applied Catalysis B: Environmental 319 (2022) 121951

Contents lists available at ScienceDirect

Applied Catalysis B: Environmental

journal homepage: www.elsevier.com/locate/apcatb

Metal-free ultrathin C_3N_5 photocatalyst coupling sodium percarbonate for efficient sulfamethoxazole degradation

Chi Ma [a,b], Zhigang Yu [c], Jingjing Wei [a,b], Chang Tan [a,b], Xu Yang [a,b], Tantan Wang [a,b], Guanlong Yu [d], Chang Zhang [a,b,*], Xin Li [a,b,*]

[a] College of Environmental Science and Engineering, Hunan University, Changsha 410082, China
[b] Key Laboratory of Environmental Biology and Pollution Control (Hunan University), Ministry of Education, Changsha 410082, China
[c] Australian Centre for Water and Environmental Biotechnology (formerly AWMC), The University of Queensland, Brisbane QLD4072, Australia
[d] School of Hydraulic and Environmental Engineering, Changsha University of Science & Technology, Changsha 410076, China

ARTICLE INFO

Keywords:
Ultrathin-C_3N_5
Sodium percarbonate
Sulfamethoxazole
Photocatalysis
Gelatin aerogel

ABSTRACT

Traditional Fenton reaction takes place at a low pH and generates waste. Additionally, the storage and transportation of liquid H_2O_2 may pose safety risks. To overcome these disadvantages, an eco-friendly, efficient advanced oxidation process was established with ultrathin-C_3N_5 photocatalyst coupling sodium percarbonate (SPC). Under visible light irradiation, up to 93.97% of SMZ was removed within 120 min. Such efficient removal was attributed to the high carriers separation efficiency of U-C_3N_5, which was certified by DFT calculations and characterization methods. All the factors (various anions, pH values, fulvic acid, light sources, and water matrices) had a slight influence on SMZ degradation. Moreover, the toxicities of SMZ and its intermediates were reduced after degradation. Finally, a gelatin aerogel/U-C_3N_5 composite was obtained to facilitate the recycling of U-C_3N_5. This work highlights the combination of metal-free photocatalysis with SPC to degrade sulfonamide antibiotics and furthers the development of advanced oxidation process for micropollutant removal.

1. Introduction

The usage of antibiotics is globally soaring, not only for human medicine but also for animal epidemic prevention. It is known that antibiotics in organisms cannot be completely absorbed and metabolized, and a large amount of them are excreted in their original form [1,2]. This leads to a high level of antibiotics entering the environment. Du et al. [3] found that twenty-five antibiotics were widely distributed in Yancheng coastal area (China), with the maximum concentration up to mg L^{-1}. Commonly used antibiotics such as sulfadiazine (SDZ), sulfamethazine (SMT), and tetracycline (TC) were detected at μg L^{-1} level in Beijing River [4]. These results imply that antibiotics are ubiquitous. Antibiotics can cause the generation of resistant strains of bacteria, leading to the altering of the bacterial community and the imbalance of the ecological environment [5,6]. Hence, it is very vital to control the concentration of antibiotics in natural water system.

As a typical advanced oxidation process (AOP), Fenton technique (hydrogen peroxide (H_2O_2) and ferrous ion (Fe^{2+})) has operational feasibility and high efficiency. It has been used for organic matter removal from wastewater [7]. However, Fenton reactions are generally effective at a relative narrow pH range (pH<3) [8] and inevitably generate red mud, a refractory solid waste [9]. It causes certain potential security risks and high economic investment in practical applications. Other oxidation systems such as peroxydisulfate or peroxymonosulfate-based AOPs have been developed with satisfactory degradation efficiency of organic matters. But the generated high concentration of sulfate ion (SO_4^{2-}) may be reduced to generate hydrogen sulfide which causes adverse effects on microorganisms [10]. In addition, sulfate radical ($SO_4^{\bullet-}$) produced from peroxydisulfate or peroxymonosulfate induce the transformation of ammonium into nitrophenolic byproducts that are hazardous [11]. Hence, a “green”, efficient, and less-cost method should be developed to remove organic matters. Photocatalysis has received a large number of interests for its high efficiency, less-cost, and eco-friendly properties. Currently, various photocatalysts have been developed, such as BiOX (X=F, Cl, Br, and I) [12–15], Cu_2O [16], C_3N_4 [17], and BiOCOOH [18], etc. Enhancing the quantum efficiency and expanding the response range of light are the main orientations to facilitate the application of photocatalysis. When

* Corresponding authors at: College of Environmental Science and Engineering, Hunan University, Changsha 410082, China
E-mail addresses: zhangchang@hnu.edu.cn (C. Zhang), hgxlixin@hnu.edu.cn (X. Li).

https://doi.org/10.1016/j.apcatb.2022.121951
Received 30 June 2022; Received in revised form 24 August 2022; Accepted 4 September 2022
Available online 7 September 2022

photocatalyst is excited with the irradiation of light (the energy of light ≥ bandgap), it can generate electron (e^-) at conduction band (CB) and hole (h^+) at valance band (VB). e^- is a reductive and h^+ is an oxidant, both of which can participate in the degradation process of pollutants. Therefore, the separation efficiency of e^-/h^+ pairs is the key factor for quantum efficiency and photocatalytic activity.

Recently, sodium percarbonate (SPC, $Na_2CO_3 \bullet 1.5\ H_2O_2$) has been used to effectively promote carriers separation and improve photocatalytic efficiency. SPC is a solid carrier of H_2O_2 and catches lots of attention due to its easy transportation, storage, and handling properties. In this case, SPC has been used as an alternative to H_2O_2 in AOPs. Similar to H_2O_2, SPC can be activated by transitional metals and ultraviolet (UV) light. In a SPC/UV system, the degradation efficiency of capsaicin reached 96.0% with 32 mmol L^{-1} SPC and 20.66 mW cm^{-2} UV intensity. While only 6.0% capsaicin was removed with alone SPC [19]. Li et al. [20] used $CuFeS_2$ activated SPC to degrade SMT. In this system, Fe^{2+} was regarded as the primary catalytic site for SPC activation and 86.4% of SMT was removed. Compared to UV and transitional metal activations that involve in the large energy consumption and the potential risks associated with metal ions release, SPC can be activated by e^- from photocatalyst, and generate active radical for contaminants degradation. Li et al. [21] used protonated g-C_3N_4 as an activator to activate SPC with the irradiation of visible light and found that the protonated g-C_3N_4/SPC/visible light possessed the highest catalytic activity in comparison to other reaction systems. A 90% of methylene blue and 70% of tetracycline hydrochloride (TC-HCl) were removed in 30 min.

The relative large bandgap (~2.7 eV) and low quantum efficiency limit the application of g-C_3N_4 in the field of photocatalytic. So some modification strategies (organic grafting [22], element loading [23], and so on) have been applied to improve the photocatalytic activity of g-C_3N_4. However, those strategies have the disadvantage of cumbersome preparation process. Compared with C_3N_4, C_3N_5, as a novel carbon nitride, with a more extended conjugated network and the participation of the lone pair on the N atom with the π conjugated system of heptazine motif possesses a smaller bandgap (1.98 eV) [24], which contributes to a wider light absorption range and higher light utilization. And its structure is shown in Fig. S1. It gets a lot of attention in the fields of environmental remediation and energy conversion [25–29]. Although C_3N_5 possesses a broad light absorption range (~700 nm), the low photocatalytic activity due to high carriers recombination efficiency needs to be overcome. Yang et al. [30] found that C_3N_4 nanosheets possessed a better carriers transfer characteristics in comparison to bulk C_3N_4. In order to enhance the quantum efficiency, our study prepared an ultrathin C_3N_5 (U-C_3N_5) by liquid phase exfoliation method and established a coupled photocatalysis-SPC system. The structure, composition, and optical characteristics of U-C_3N_5 were analyzed by various advanced techniques such as field-emission transmission electron microscopy (FETEM), X-ray diffraction (XRD), and photoluminescence (PL). In addition, Density Functional Theory (DFT) calculation was also applied to further elaborate the physicochemical property of U-C_3N_5. The activation efficiency of SPC by U-C_3N_5 was investigated via the degradation of sulfamethoxazole (SMZ) under visible light irradiation. The dominant reactive oxygen species for SMZ degradation and the reaction mechanisms of the U-C_3N_5/SPC/Visible light process were revealed. The degradation pathways and the toxicities of intermediates were analyzed. The practicability of the U-C_3N_5/SPC/Visible light process was also evaluated under various light sources, water matrices, pH values, different anions, and so on. Finally, a self-suspension gelatin aerogel loaded U-C_3N_5 photocatalyst (U-C_3N_5/GA) was obtained in order to facilitate the recovery of U-C_3N_5. Collectively, this work provides a metal-free U-C_3N_5 photocatalyst and a combination of metal-free photocatalysis with SPC to degrade sulfonamide antibiotics and advances the technique for emerging pollutants removal from water and wastewater.

2. Materials and methods

2.1. Reagents

Melamine ($C_3H_6N_6$, CP), tert-butanol ($C_4H_{10}O$, TBA, CP) and gelatins (CP) all got from Sinopharm Chemical Regent Co., Ltd. Sodium percarbonate ($Na_2CO_3 \bullet 1.5\ H_2O_2$, SPC, ≥ 13.0% active oxygen) was obtained from Aladdin Reagent Co., Ltd. 3-Amino-1,2,4-triazole ($C_2H_4N_4$, 98%) was got from Shanghai Yien Chemical Technology Co., Ltd. Sulfamethoxazole ($C_{10}H_{11}N_3O_3S$, SMZ, 98%) was obtained from Adamas Reagent Co., Ltd. CP represents chemical pure. Other reagents were displayed in Supplementary Information. All the reagents were used as received without further purification.

2.2. Photocatalysts synthesis and characterizations

C_3N_5 was successfully prepared according to the method of Zhang et al. [24]. And the detailed information on photocatalysts synthesis and characterization was provided in Supplementary Information. Typically, the morphological features were observed via FETEM and atomic force microscope (AFM). And the phase structure and surface chemical composition were studied by XRD and X-ray photoelectron spectroscopy (XPS).

2.3. DFT calculations

In this work, the first-principles calculation steps were completed through structural optimization, static self-consistent field, density of state calculation, and charge calculation. The detailed information was provided in Supplementary Information.

2.4. Experiment procedures

The performance of SMZ degradation by the photocatalyst/SPC/Light system was investigated (Fig. S2). A 300 W xenon lamp (PLS-SXE300/300UV, Beijing Perfectlight Technology Co., Ltd.) equipped with 420 nm cut-off filter was worked as a visible light source and a 30 W LED light (QIAO KU, QKT30W) was worked as a LED light source. A circulating water system was used to keep the reaction temperature at 25 ± 0.5 °C. Initially, the photocatalyst (20 mg) was put into 100 mL 10 mg L^{-1} (To facilitate detection, the concentration of SMZ was set to 10 mg L^{-1}.) SMZ solution and sonicated for 5 min to disperse the photocatalyst. Then, 10 mg of SPC was put into the mixed solution. Priority to the reaction, the mixture was stirred for 30 min in the darkness to achieve the equilibrium of the adsorption-desorption reaction. The degradation reaction was started by turning on the light and 1.5 mL of the reaction solution was withdrawn at a certain time and filtered with 0.22 μm syringe filter to remove the photocatalyst. The concentration of residual SMZ was measured via high performance liquid chromatography (HPLC, Agilent Technologies 1260 Infinity II) with an ultraviolet detector (Test condition was shown in Table S1). To estimate the reusability of U-C_3N_5, the used U-C_3N_5 was recycled by filtration and rinsed with deionized water and ethanol. To investigate the reactive species, the trapping experiments were conducted with the addition of various sacrificial agents (isopropanol (IPA) and TBA for hydroxyl (•OH), furfuryl alcohol (FFA) for singlet oxygen ($^1O_2$), phenol for •OH and carbonate radical ($\bullet CO_3^-$), p-benzoquinone (BQ) for superoxide radical ($\bullet O_2^-$), EDTA-2Na and triethanolamine (TEOA) for h^+). Other contaminants (TC-HCl, bisphenol A (BPA), naproxen (NPX), 2, 4-dichlorophenol (2,4-DCP), and ciprofloxacin (CIP)) were also degraded with the same experimental conditions. Three-dimensional excitation-emission matrix spectroscopy (3D-EEMs) and liquid chromatography-mass spectrometry (LC-MS) were applied to analyze intermediates (Test condition was shown in Table S2). All experiments were conducted in triplicates.

To estimate the toxicity of intermedia products, we tested with *Escherichia coli* (*E. coli*, DH5α). Firstly, *E. coli* cells were activated by

inoculating and culturing in Luria-Bertani liquid medium at 37 °C for 8 h in a constant temperature incubator shaker with 150 rpm. Then 30 μL of activated *E. coli* was inoculated to the mixed solution composed of Luria-Bertani liquid medium and SMZ degradation solution at 0, 1, 2, and 4 h and residual photocatalyst was removed by 0.22 μm filter. The optical density (OD_{600}) of cell suspension was recorded at 600 nm by UV–vis spectrophotometer after 6 h incubation at 37 °C. A blank experiment was conducted with the mixed solution of deionized water and Luria-Bertani liquid medium. The optical density of water was marked as $OD_{600(water)}$.

3. Results and discussion

3.1. Characterizations of the obtained photocatalysts

The morphological features of U-C_3N_5, C_3N_5, U-C_3N_4, and C_3N_4 were observed via FETEM and AFM. It was obvious that a stacked nanosheets structure was obtained and the size of U-C_3N_5 was the smallest (Fig. 1 (a)-(d)). In addition, no distinct crystallite fringes were observed from the high resolution-TEM images of all the obtained photocatalysts (Fig. 1 (e)-(h)). Furthermore, the thickness of nanosheets of the obtained samples was measured by AFM. The thickness of U-C_3N_5 and C_3N_5 was about 0.3 and 2.0 nm (Fig. 1(i), (j) and Fig. S3), indicating that an ultrathin C_3N_5 was indeed obtained via sonicating.

The phase structure and surface chemical composition of the obtained samples were studied by XRD and XPS. All the samples had two distinct diffraction peaks (Fig. 2(a)). The diffraction peaks located at 12.48° and 27.56° belonged to (100) and (002) plane, respectively [27, 31]. The XPS elemental survey scan of C_3N_5 and U-C_3N_5 displayed three peaks related to C 1 s, N 1 s, and O 1 s (Fig. 2(b)), which further confirmed the obtained C_3N_5. The existence of O might come from H_2O or/and CO_2 which was adsorbed. The C 1 s high resolution XPS spectrum of U-C_3N_5 and C_3N_5 were deconvolved into four peaks (Fig. 2(c)). The peaks at binding energies of 284.84, 287.88, and 288.48 eV belonged to adventitious carbons, N-C═N group, and C-NH_2 group, respectively. Additionally, the peak located at 294.16 eV was attributed to π-π * [32]. The N 1 s high resolution XPS spectrum of U-C_3N_5 and C_3N_5 were deconvolved into three peaks at 398.75, 400.42, and 404.94 eV (Fig. 2 (d)), which were assigned to C-N═C, C-NH_2/C-N═N-C, and π-π *, respectively [24]. These results also showed minor differences in the intensity of XRD and XPS between U-C_3N_5 and C_3N_5. This result implied that there was no obvious difference between U-C_3N_5 and C_3N_5 in structure and composition. In addition, the XPS spectrum of U-C_3N_4 and C_3N_4 were displayed in Fig. S4. In order to confirm the atomic rate of C : N, a CHN elements analysis was applied. The result of CHN elements analysis showed that the weight percentages of C : N was 33.40% : 58.73%. And the C : N atomic ratio was calculated to be 0.6635, which was close to the theoretical value (0.6000). Taken together, these results demonstrated that C_3N_5 was successfully synthesized.

To distinguish the difference between U-C_3N_4 and U-C_3N_5, fourier transform infrared (FTIR) spectroscopy, Raman spectra, and electron energy loss spectroscopy (EELS) were applied and further explained the difference between U-C_3N_5 and U-C_3N_4. As Fig. 3(a) shown, the broad peak at 3175 cm^{-1} is ascribed to the -NH_2 or/and -OH stretch vibrations. The peaks at 1636–1239 cm^{-1} are attributed to the triazine ring stretch. The peaks at 890 and 808 cm^{-1} are related to the bending vibrations of

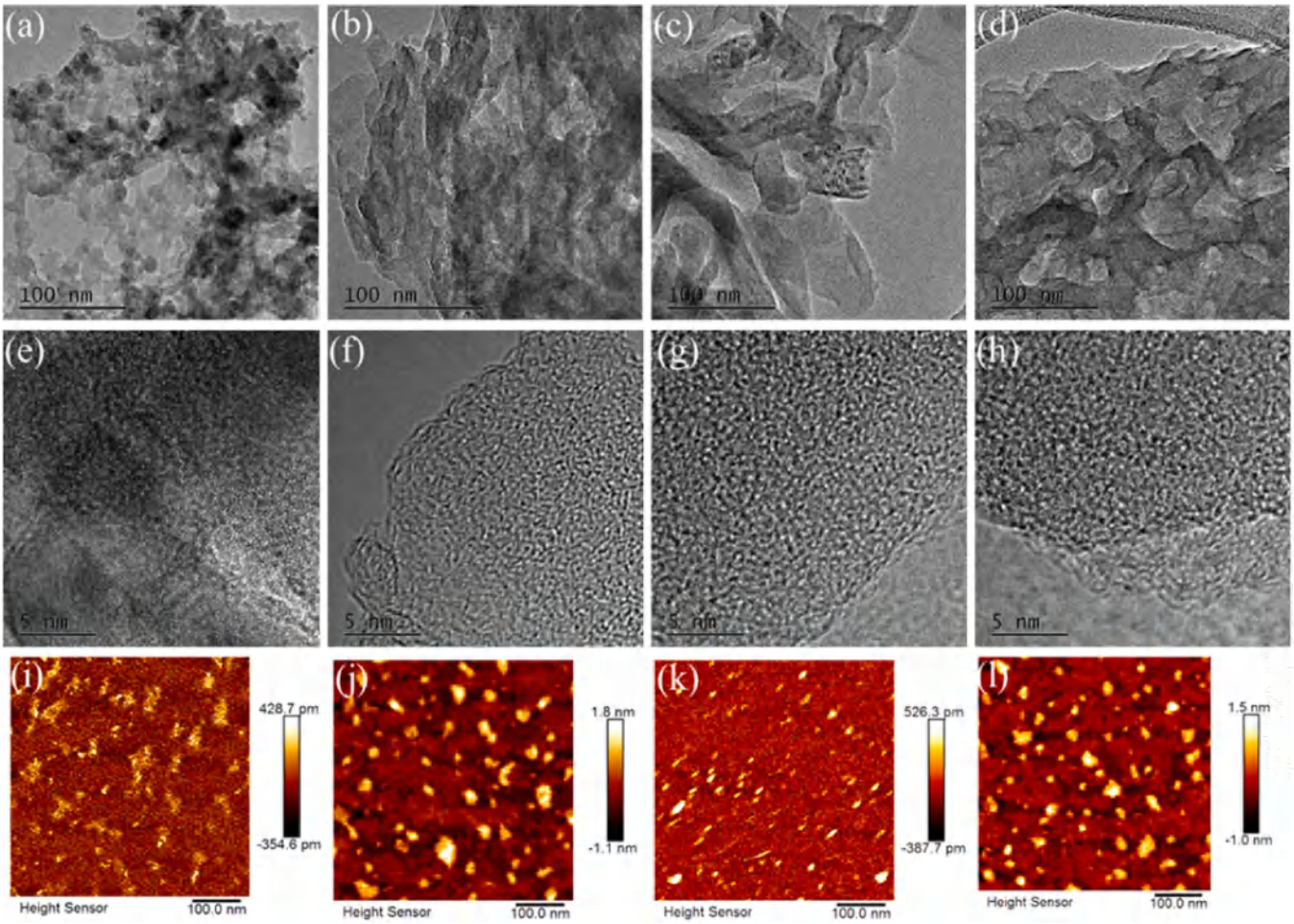

Fig. 1. The FETEM and AFM images of U-C_3N_5(a, e, and i), C_3N_5(b, f, and j), U-C_3N_4(c, g, and k), and C_3N_4(d, h, and l).

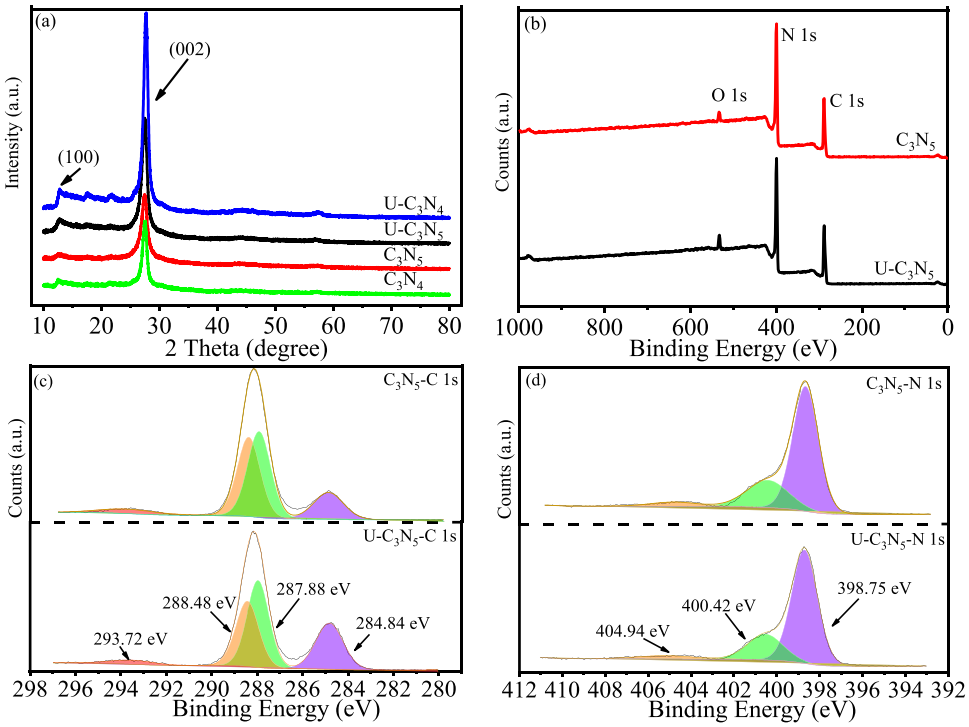

Fig. 2. The XRD and XPS of the obtained samples.

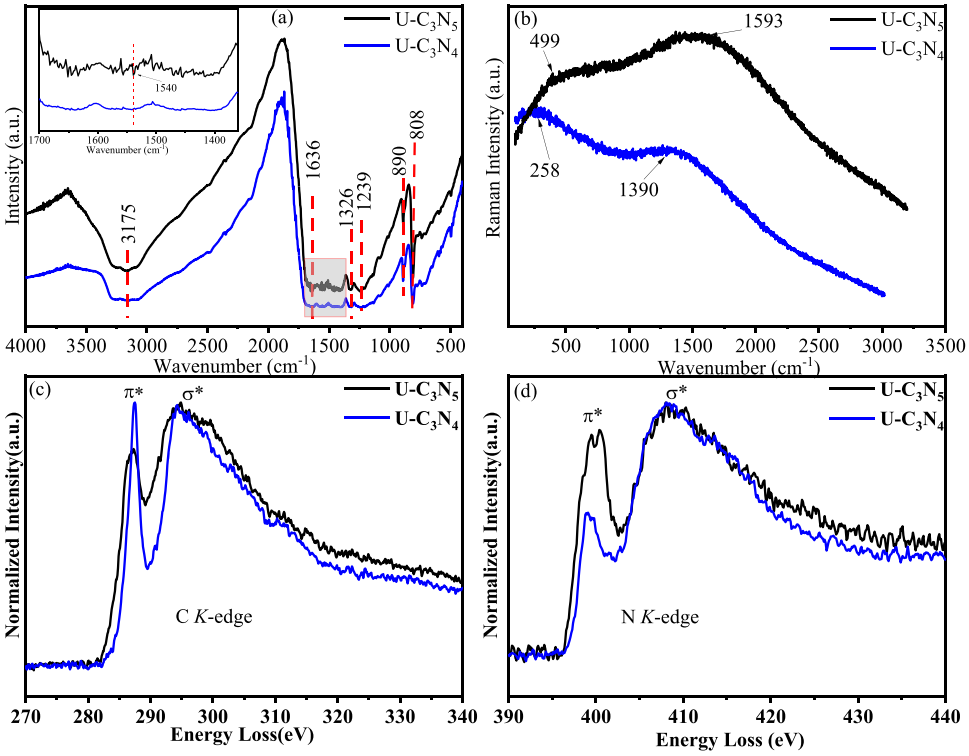

Fig. 3. The FTIR spectra (a), raman spectra (b) and ELLS spectra ((c), (d)) of U-C_3N_4 and U-C_3N_5.

N-H [31]. In addition, the FTIR spectrum of U-C_3N_5 appear some new weak peaks around 1540 cm^{-1} implicating the tertiary amine stretch. The Raman spectra of U-C_3N_4 and U-C_3N_5 have no obvious characteristic peaks (Fig. 3(b)), which may be caused by the fluorescence of the material. In order to clarify the nature of N and C bonding in U-C_3N_4 and U-C_3N_5, EELS was conducted. The C K-edges signal of U-C_3N_4 and U-C_3N_5 contained two peaks located at 287.6 and 294.4 eV related to 1 s-π * and 1 s-σ * electronic transition of sp^2 hybridized carbons (Fig. 3 (c)) [33]. The N K-edges loss peaks for U-C_3N_4 and U-C_3N_5 mainly located at 399.4 and 408.2 eV corroborated to 1 s-π * and 1 s-σ * electronic transition of sp^2 hybridized nitrogens in heptazine and bridging N (Fig. 3(d)). And a new peak at 400.5 eV in N K-edge loss of

U-C_3N_5 indicated a new electronic environment of N (tertiary amine N) [34]. Compared with the N K-edge π * of U-C_3N_4, the relative high peak intensity of the N K-edge π * of U-C_3N_5 implied that decreased contribution of N-N in 1 s-σ * transition. The replacement of N-N increased a lone pair, which contributes to π * signal. The total peak area of the N K-edge peak for U-C_3N_5 was increased in comparison to U-C_3N_4, which implied addition of extra nitrogens in the U-C_3N_5 [31]. The atomic content of C and N measured in U-C_3N_5 and U-C_3N_4 were about 43%, 57%, 55%, and 45% (Fig. S5), respectively. The atomic content of N in U-C_3N_5 was about 10% higher than that in U-C_3N_4, indicating the high N content in U-C_3N_5. Compared with the theoretical value of C : N ratio in U-C_3N_5 and U-C_3N_4, the higher C : N ratio of experimental value was attributed to the added C in the sample substrate.

3.2. SMZ degradation and mechanism analysis

As shown in Fig. 4(a), SMZ could not be degraded after 120 min of reaction in the SPC/Dark, SPC/Light, and U-C_3N_5/SPC/Dark systems, respectively. These results implied that SPC, U-C_3N_5 or visible light alone cannot oxidize SMZ. However, SMZ was degraded in an alone photocatalytic system (U-C_3N_5/Light), and 38.08% of SMZ was removed, indicating that U-C_3N_5 could generate e^-/h^+ pairs with the irradiation of visible light. Remarkably, when SPC combination with photocatalytic system (U-C_3N_5/SPC/Light), a much higher degradation efficiency of SMZ was achieved, with 76.23% of SMZ removed in 120 min. In addition, the degradation rate constant was calculated via Eq.(1). Where C_0 and C_t are the concentration of SMZ at 0 and t min, respectively. k (min^{-1}) is rate constant. t (min) is reaction time. The degradation reaction of SMZ was well fitted with pseudo first order reaction, and the rate constant of U-C_3N_5/SPC/Light (0.0118 min^{-1}) was 3.37 times than that of U-C_3N_5/Light (0.0035 min^{-1}) (Fig. 4(b) and Table S3). In addition, we compared with other literatures for the degradation of SMZ (Table S4). As Table S4 displayed, the degradation rate and k of SMZ for U-C_3N_5/SPC/Light are better than that of other materials which prepared in other literatures with the same conditions.

$$\ln(C_t/C_0) = -kt \quad (1)$$

The degradation of SMZ by C_3N_5, U-C_3N_4, and C_3N_4 was also carried out with the same experimental conditions. As depicted in Fig. 4(c), (d) and Table S5, the removal efficiency of SMZ were 55.06% (0.0065 min^{-1}), 41.43% (0.0041 min^{-1}), and 27.31% (0.0024 min^{-1}) for C_3N_5/SPC/Light, U-C_3N_4/SPC/Light, and C_3N_4/SPC/Light, respectively. These results demonstrated that the photocatalytic activity followed the order: U-C_3N_5 > C_3N_5 > U-C_3N_4 > C_3N_4.

In order to explore the underlying mechanisms of excellent catalytic activity of U-C_3N_5, a series of photoelectric characteristics tests were carried out. As Fig. 5(a) demonstrated, U-C_3N_5 could absorb light that the wavelength varied from 200 to 800 nm. And the light response range of U-C_3N_5 and C_3N_5 was wider than that of U-C_3N_4 and C_3N_4. Accordingly, the light response range of C_3N_5 was wider than that of U-C_3N_5. The bandgaps of U-C_3N_5, C_3N_5, U-C_3N_4, and C_3N_4 were calculated to be 2.02, 1.62, 2.36, and 2.28 eV according to the plots of hν versus $(\alpha h\nu)^{1/2}$, respectively (Fig. 5(b)). Where h is the Planck constant, ν is light frequency, and α is a constant. The bandgaps were well fit with the results of UV–vis DRS. According to the results of UV–vis DRS, C_3N_5 would possess the best catalytic activity, which was not consistent with the experimental result. In order to clarify the internal factors, PL spectrum was conducted to investigate the separation efficiency of e^-/h^+ pairs. A 377 nm light source was worked as the exciting source. Generally, a high PL intensity implies a high recombination efficiency of e^-/h^+ pairs [35]. As Fig. 5(c) displayed, U-C_3N_4 and C_3N_4 displayed an intense emission peak at 466 nm and the emission peak intensity of C_3N_4 was stronger than that of U-C_3N_4, which suggested the fast recombination of e^-/h^+ pairs in C_3N_4 [36]. By contrast, U-C_3N_5 and C_3N_5 did not occur distinguishing PL emission peak, which implied an efficient separation of e^-/h^+ pairs between the surface and bulk in U-C_3N_5 and C_3N_5. What's more, the PL emission peak intensity of U-C_3N_5 was weaker than that of C_3N_5, which indicated a more efficient separation of e^-/h^+ pairs of U-C_3N_5 than that of C_3N_5 [31]. In order to further explore the separation processes of carriers, the time-resolved PL spectrum of all the obtained samples was collected (Fig. 5(d)). The PL decay curve was matched

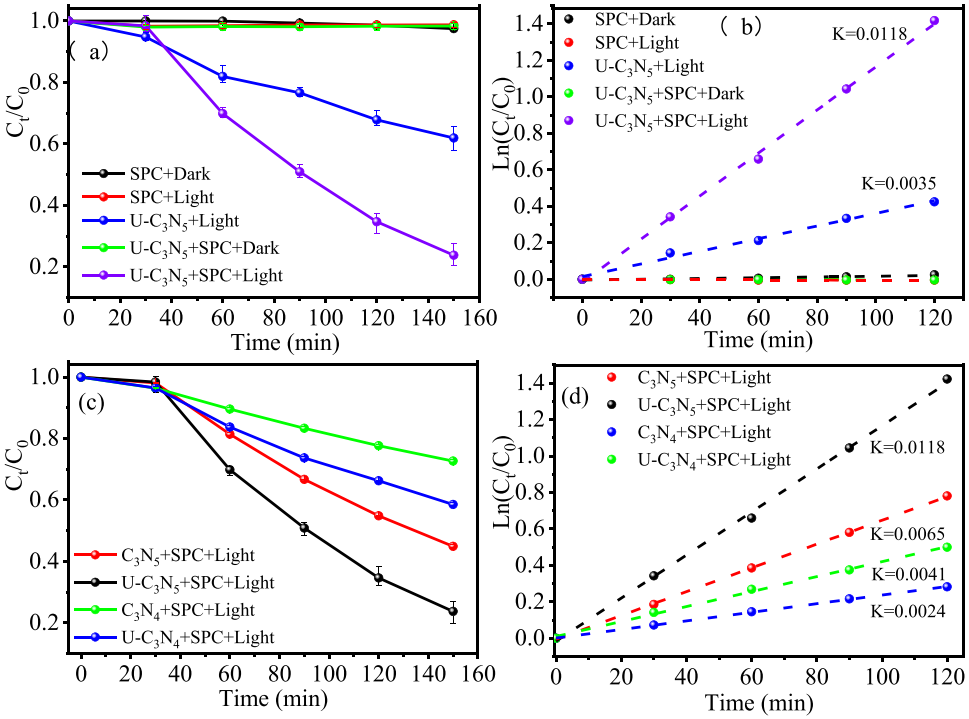

Fig. 4. Degradation of SMZ (a) and (c), the corresponding k values (b) and (d). Experimental conditions: $C_{SMZ,\ initial}$= 10 mg L^{-1}, $C_{photocatalyst}$= 200 mg L^{-1}, C_{SPC}= 100 mg L^{-1}, T = 25 ± 0.5 °C, visible light.

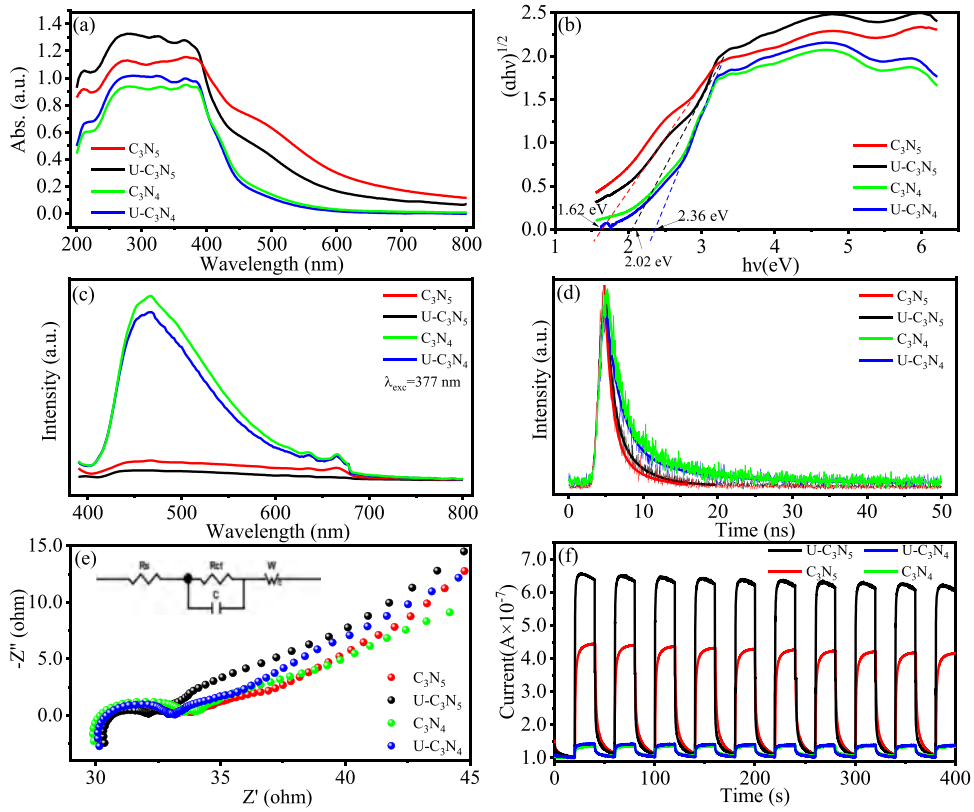

Fig. 5. Photoelectric performance tests. (a) UV–vis diffuse reflectance spectra, (b) a plot of $(\alpha h\nu)^{1/2}$ versus hν, (c) PL spectra, (d) Photoluminescence lifetime decay curves, (e) EIS Nyquist plots, and (f) Photocurrent densities.

sec-exponentially (Eq.(2)).

$$I(t) = B_1 e^{-t/\tau_1} + B_2 e^{-t/\tau_2} \quad (2)$$

Where B_1 and B_2 are the normalized amplitudes of each decay component. τ_1 and τ_2 are values of the radiation lifetimes [37]. The average lifetime (τ_{avg}, Eq. (3)) is deemed as a coherent measure to estimate the rate of spontaneous emission.

$$\tau_{avg} = (B_1\tau_1^2 + B_2\tau_2^2)/(B_1\tau_1 + B_2\tau_2) \quad (3)$$

The obtained values of lifetimes and average lifetime were presented in Table S6. The average lifetime of U-C_3N_5 (3.1743 ns) was the smallest among all the obtained samples, which implied that a fast quenching of

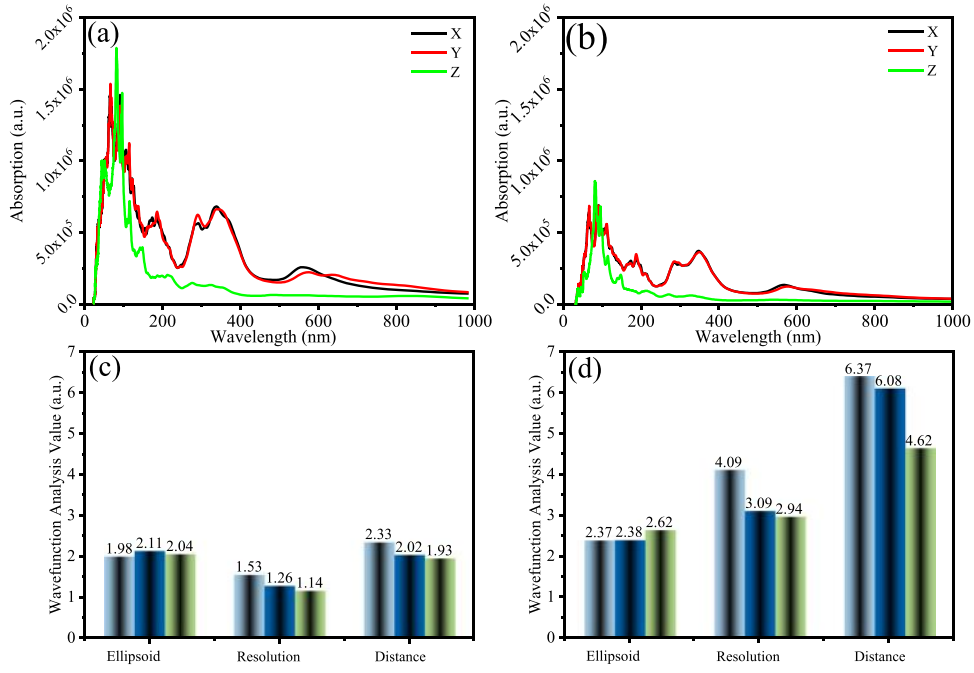

Fig. 6. The light absorption and electron-hole separate degree of ellipsoid, resolution and distance of C_3N_5 ((a), (c)) and U-C_3N_5 ((b), (d)).

the U-C_3N_5 luminescence occurred. The weak PL intensity and small average lifetime manifested the excellent charge separation efficiency in U-C_3N_5 [31]. Additionally, a series of photo-electrochemical tests were also carried out to study the e^-/h^+ pairs separation characteristics. The results of electrochemical impedance spectroscopy (EIS) showed that the arc radius of U-C_3N_5 was the smallest (Fig. 5(e)), indicating the lowest electron transfer resistance of U-C_3N_5 [38]. At the same time, the Nyquist diagram was fitted to the simplified circuit, and the series resistance (Rs) and charge transfer resistance (Rct) were extracted. As the simplified circuit diagram shown (Fig. 5(e) inset), it consists of three series resistances (Rs, Rct, and W) and a parallel capacitor (C). And the values of Rs and Rct were shown in Table S7. It was obvious that the value of Rct of U-C_3N_5 was the minimum (0.97 Ω). This was consistent with the results of photocurrent densities (Fig. 5(f)), where U-C_3N_5 exhibited the highest photocurrent densities. Thus, these results suggest that U-C_3N_5 shows superior e^-/h^+ pairs separation efficiency [39].

In addition, DFT calculations were also applied to clarify the excellent activity of U-C_3N_5. As shown in Fig. 6(a) and (b), the light absorption ability of C_3N_5 was stronger than that of U-C_3N_5 in the XYZ three directions, which was consistent with the results of UV–vis DRS. The e^-/h^+ pairs separation degree of C_3N_5 and U-C_3N_5 were illustrated by ellipsoid, resolution and distance. All of the ellipsoid, resolution and distance of U-C_3N_5 were bigger than that of C_3N_5 (Fig. 6(c) and (d)), which implied that U-C_3N_5 shows superior e^-/h^+ pairs separation efficiency [40,41]. These results were in good agreement with experimental results.

Moreover, we investigated the influence of several factors including the dosage of U-C_3N_5 and SPC, anions, and the initial pH on SMZ degradation. As revealed in Fig. 7(a), the degradation efficiency of SMZ elevated from 56.84% to 81.08% with the concentration of SPC increased from 50 to 200 mg L^{-1}, and the corresponding rate constants gradually elevated from 0.0069 to 0.0133 min^{-1} (Fig. 7(b) and Table S8). The enhanced removal efficiency might be ascribed to the generation of more reactive species with higher dosage SPC. However, the removal rate decreased to 76.96% with 300 mg L^{-1} SPC. This might be attributed to the superfluous SPC, leading to an excessive H_2O_2 that could work as a •OH scavenger, as displayed by Eqs.(4), (5) [42,43].

$$\bullet OH + H_2O_2 \rightarrow \bullet OOH + H_2O \quad (4)$$

$$\bullet OH + \bullet OOH \rightarrow O_2 + H_2O \quad (5)$$

Similarly, the degradation efficiency of SMZ increased from 54.45% to 93.97% with the dosage of U-C_3N_5 increased from 10 to 40 mg (Fig. 7(c)). Correspondingly, the rate constants boosted from 0.0062 to 0.0230 min^{-1} (Fig. 7(d) and Table S9). The enhanced removal efficiency might be attributed to the more e^-/h^+ pairs for activation of SPC with a high U-C_3N_5 dosage. However, the removal efficiency decreased from 93.97% to 84.08% when further increasing the U-C_3N_5 dosage from 40 to 60 mg. As the superfluous U-C_3N_5 could induce a shielding effect and may restrict the penetration of light, leading to less U-C_3N_5 activated and less e^-/h^+ pairs generated to activate SPC.

The catalytic efficiency was also related to the original pH of the solution. As Fig. 7(e) shown, the removal efficiency of SMZ increased from 73.69% to 82.97% with the pH increased from 3.00 to 7.08. But the efficiency decreased from 82.97% to 78.14% when the pH was increased from 7.08 to 9.17. This is because at high pH (> 7.0), the oxidation potential of •OH is low and H_2O_2 can be self-decomposed into O_2 and H_2O [44,45]. When the pH < 7.0, U-C_3N_5 was positively charged (Fig. S6), while SMZ existed as neutral or amphoteric species (pH = 3.00, pK_{a1}=1.85; pH = 5.31, pK_{a2}=5.60). The weak interaction between SMZ and U-C_3N_5 restricted the degradation of SMZ, thus leading to a low degradation efficiency of SMZ at low pH levels.

The anions and dissolved organic matter are ubiquitous in actual water, which may have an influence on the degradation efficiency of

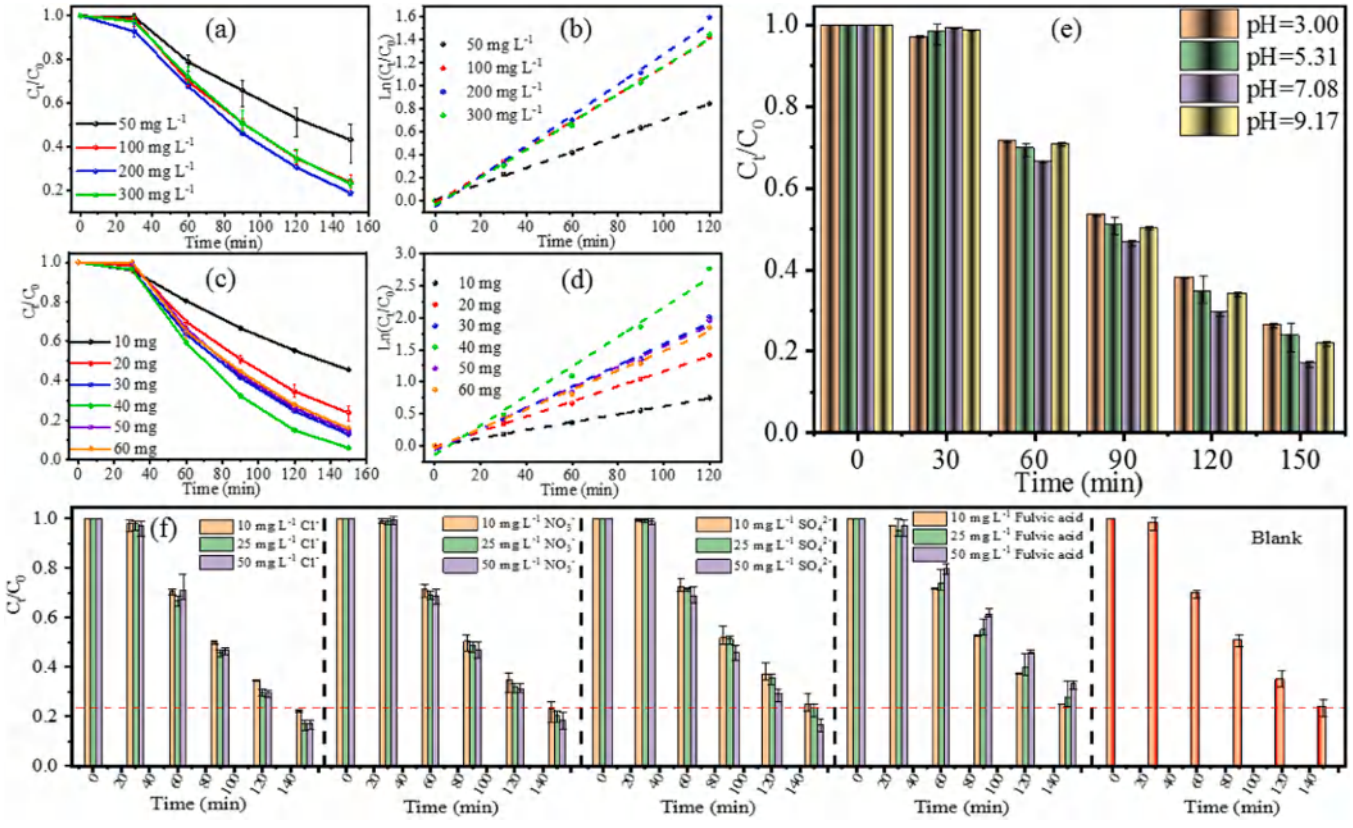

Fig. 7. The influence factors on SMZ degradation: (a) SPC concentration, (c) U-C_3N_5 dosage, (e) the initial pH of SMZ solution, (f) anions (Cl^-, NO_3^-, and SO_4^{2-}) and fulvic acid, (b) and (d) the k values of SPC concentration and U-C_3N_5 dosage. Experimental conditions: $C_{SMZ,\ initial}$= 10 mg L^{-1}, T = 25 ± 0.5 °C, visible light.

SMZ. Herein, the effects of various anions (Cl^-, NO_3^-, and SO_4^{2-}) and fulvic acid on SMZ degradation were investigated. As Fig. 7(f) demonstrated, a low concentration of anions (10 mg L^{-1}) almost did not affect the degradation of SMZ. Surprisingly, a slight enhancement in SMZ degradation was achieved with the relative high anions concentrations (25 and 50 mg L^{-1}). Noted that Cl^- and SO_4^{2-} are easy to be oxidized by •OH and to form active species (Eqs.(6)-(13)) [46,47]. In addition, NO_3^- has a photochemical activity and can generate $•NO_2$ and •OH with the irradiation of light (Eqs.(14), (15)) [48]. It was obvious that fulvic acid suppressed the degradation of SMZ, which was attributed to the competitive effect of fulvic acid and SMZ [49].

$$Cl^- + • OH \rightarrow Cl^• + OH^- \quad (6)$$

$$Cl^• + Cl^- \leftrightarrow •Cl_2^- \quad (7)$$

$$Cl^• + H_2O_2 \rightarrow H^+ + Cl^- + HO_2• \quad (8)$$

$$•Cl_2^- + H_2O_2 \rightarrow H^+ + 2Cl^- + HO_2• \quad (9)$$

$$SO_4^{2-} + H^+ \rightarrow HSO_4^- \quad (10)$$

$$HSO_4^- + • OH \rightarrow •SO_4^- + H_2O \quad (11)$$

$$•SO_4^- + H_2O \rightarrow H^+ + SO_4^{2-} + • OH \quad (12)$$

$$•SO_4^- + H_2O_2 \rightarrow SO_4^{2-} + H^+ + H_2O• \quad (13)$$

$$NO_3^- + h\upsilon \rightarrow •NO_2 + •O^- \quad (14)$$

$$•O^- + H_2O \rightarrow • OH + OH^- \quad (15)$$

The stability of catalysts plays a crucial role in practical applications. As Fig. 8(a) displayed, the removal efficiency of SMZ slightly declined in five cycles, which might be due to the loss of U-C_3N_5 and competitive adsorption of intermediates and/or residual SMZ on the surface of U-C_3N_5 [24]. In order to further examine the stability of U-C_3N_5, XRD and XPS of used U-C_3N_5 were also measured. The XPS data of the fresh and used U-C_3N_5 were unchanged (Fig. 8(b)-(d)). Similarly, the XRD patterns of the fresh and used U-C_3N_5 were identical except for the peak intensity was slightly weaker (Fig. 8(e)). All of these results implied that U-C_3N_5 exhibits good stability against SMZ degradation over serval hours.

To elucidate the reaction mechanism, a series of quenching tests were carried out to probe dominant active species in the U-C_3N_5/SPC/Visible light system. We found that the degradation efficiency of SMZ was not changed with the addition of •OH scavenger (5 mM IPA or TBA, Fig. 9(a)). By contrast, the removal efficiency of SMZ decreased from 79.81% to 66.31%, when 100 mM TBA was added. This result implied that •OH took part in the degradation of SMZ. The h^+, an oxidant, on the VB of U-C_3N_5 was generated with the irradiation of visible light, and it also might take part in the reaction. Herein, TEOA and EDTA-2Na were used to study the influence of h^+ on the degradation of SMZ. When 5 mM TEOA or EDTA-2Na was added, the degradation efficiency of SMZ dramatically declined. In addition, BQ, FFA, and phenol that separately capture $•O_2^-$, $^1O_2$, and both $•CO_3^-$ and •OH, decreased the degradation efficiency of SMZ. These results confirmed that •OH, h^+, $•O_2^-$, $^1O_2$, and $•CO_3^-$ were all involved in the degradation of SMZ. To further confirm the existence of these active species, electron spin resonance (ESR) spectra were recorded. The characteristic peaks of $•O_2^-$, $^1O_2$, •OH, and $•CO_3^-$ were detected with the irradiation of visible light (Fig. 9(b)). We also found that the peak intensity of U-C_3N_5 was the strongest (Fig. 9(b) and Fig. S7), which implied that the U-C_3N_5/SPC/Visible light system generated the highest levels of these active species. At the same time, the peak intensity of C_3N_5 was stronger than that of C_3N_4. What's more, there were no characteristic peaks of all active species of all the obtained samples in the darkness, which implied that SPC could not be activated by all the obtained samples without the irradiation of light. These results were consistent with the experimental data (Fig. 4). Collectively, we proposed underlying mechanisms of SMZ degradation by U-C_3N_5/SPC/Visible light (Fig. 9(c)). First, e^-/h^+ pairs were generated from visible light excited U-C_3N_5 (Eq.(16)). The potential of e^- and h^+ were calculated according to the Mott-Schottky curve (Fig. S8) and UV–vis DRS. As original active species, e^- had two ways to take part in the next reactions. The first one was that e^- reacted with O_2 to generate $•O_2^-$ (Eq.(17))

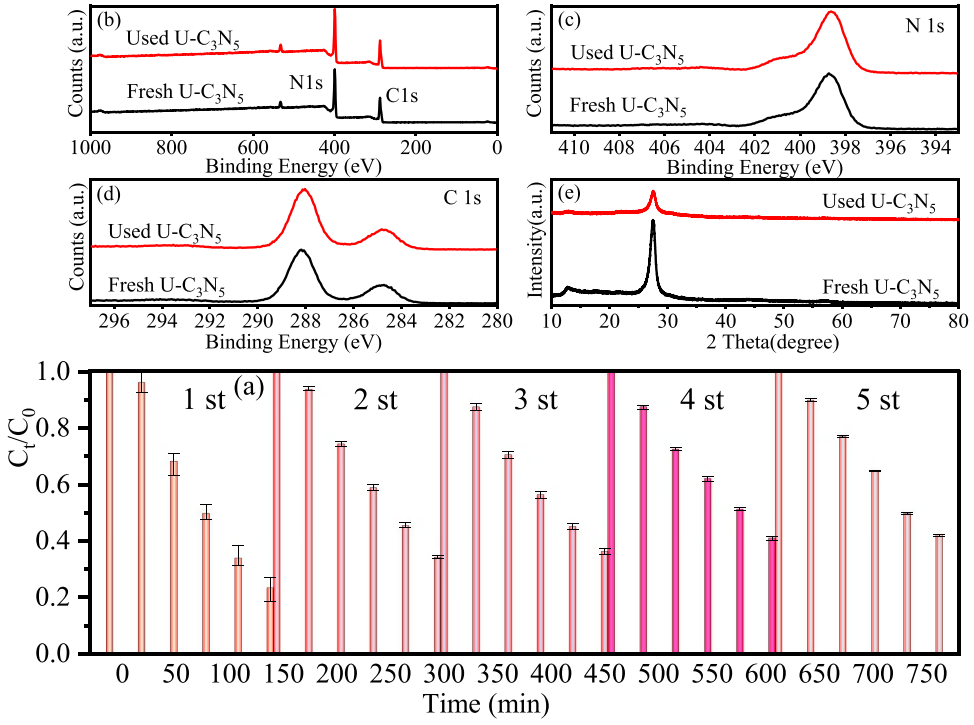

Fig. 8. The recycle runs of SMZ degradation using the U-C_3N_5/SPC/Visible light system (a), the XPS spectrums of fresh and used U-C_3N_5 (b)-(d), XRD patterns of fresh and used U-C_3N_5 (e).

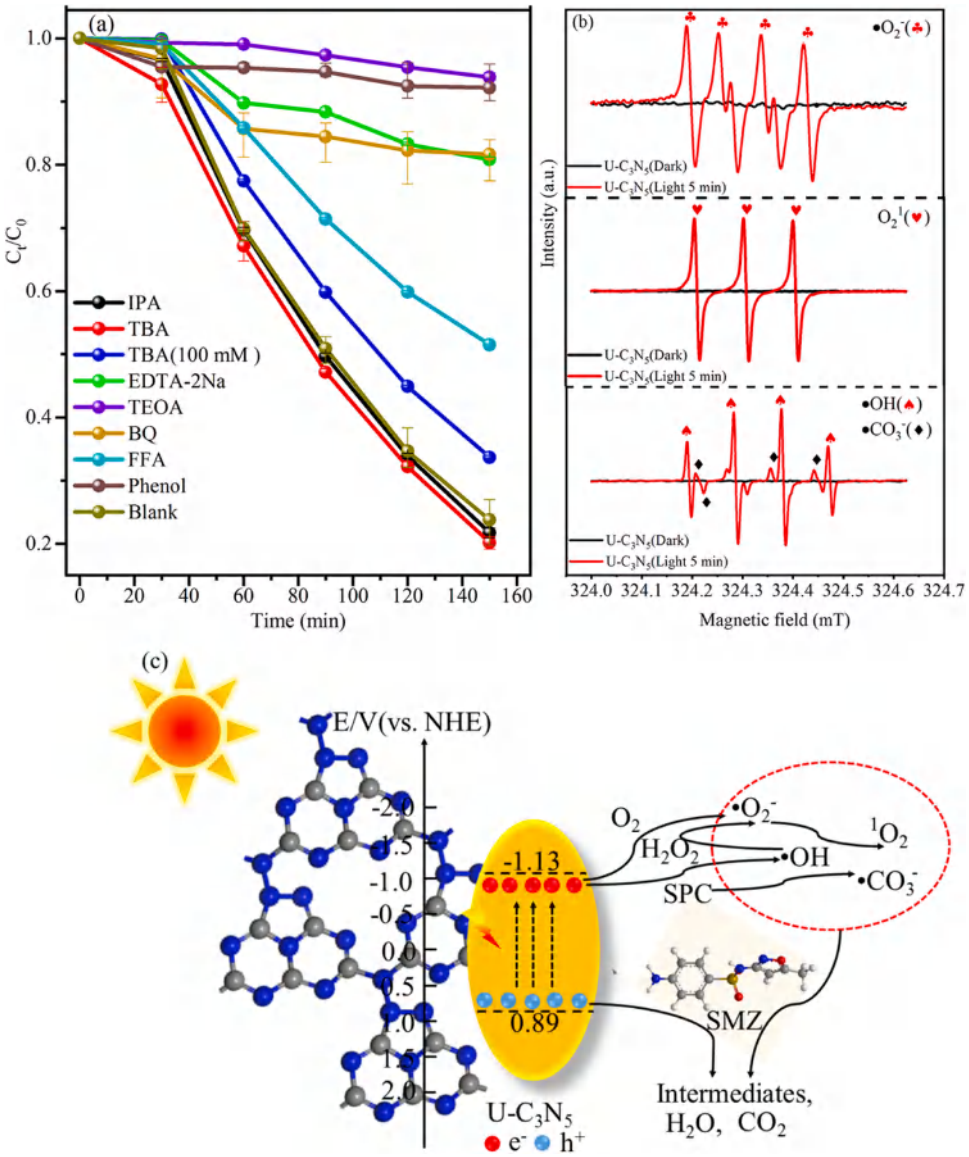

Fig. 9. The effects of scavengers on SMZ degradation in the U-C_3N_5/SPC/Visible light system (a), experimental conditions: $C_{SMZ,\ initial}$= 10 mg L^{-1}, $C_{photocatalyst}$= 200 mg L^{-1}, C_{SPC}= 100 mg L^{-1}, T = 25 ± 0.5 °C, visible light; ESR spectra of active species (b); the possible reaction mechanism of U-C_3N_5/SPC/Visible light system (c).

because the CB potential (−1.13 V vs. NHE) of U-C_3N_5 was more negative than that of $O_2/\bullet O_2^-$ (−0.33 V vs. NHE). Additionally, $\bullet O_2^-$ can also be generated by Eq.(20) [50]. The other way was that e^- reacted with H_2O_2 which was produced via decomposing of SPC to generate •OH (Eqs.(18), (19)). Since the potential of VB (0.89 V vs. NHE) of U-C_3N_5 was less positive than that of $\bullet OH/OH^-$ (1.99 V vs. NHE) and $\bullet OH/H_2O$ (2.27 V vs. NHE), h^+ could not oxidize OH^- or H_2O to generate •OH. Moreover, according to the results of quenching experiments and ESR, $^1O_2$ and $\bullet CO_3^-$ all participated in the SMZ degradation process and could be produced via Eqs.(21)-(23) [51].

$$U - C_3N_5 + visible \quad light \rightarrow e^-(CB) + h^+(VB) \tag{16}$$

$$e^-(CB) + O_2 \rightarrow \bullet O_2^- \tag{17}$$

$$Na_2CO_3 \bullet 1.5H_2O_2 \rightarrow Na_2CO_3 + 1.5H_2O_2 \tag{18}$$

$$2e^- + H_2O_2 \rightarrow 2 \bullet OH \tag{19}$$

$$H_2O_2 + \bullet OH \rightarrow \bullet O_2^- + H^+ + H_2O \tag{20}$$

$$\bullet O_2^- + \bullet OH \rightarrow {}^1O_2 + OH^- \tag{21}$$

$$2 \bullet O_2^- + 2H^+ \rightarrow {}^1O_2 + H_2O_2 \tag{22}$$

$$CO_3^{2-} + \bullet OH \rightarrow \bullet CO_3^- + OH^- \tag{23}$$

3.3. The degradation pathways and intermediates toxicities evaluation of SMZ

The mineralization rate of SMZ was assessed by total organic carbon (TOC) measurement. As Fig. S9 displayed, only 67.06% of TOC was removed in 240 min, whereas SMZ was almost completely removed. These results indicated that there were many intermediates not completely decomposed. In order to assess the potential cytotoxicity of SMZ and its intermediates, *E. coli* (DH5α) was used as the target bacterium and the optical density at 600 nm (OD_{600}) of *E. coli* (DH5α) was measured. It was clear that the growth of *E. coli* (DH5α) was slightly restrained by the addition of the initial SMZ solution. The growth of *E. coli* (DH5α) was obviously arrested at 60 and 120 min. What's more,

the inhibiting effect disappeared with the addition of reaction solution at 240 min. The result of the cytotoxicity test manifested that the generated intermediates were poisonous. And the toxicities of the intermediates could be reduced when the reaction was complete.

In order to clarify the intermediate products and degradation pathways more intuitively, 3D-EEMs and LC-MS were carried out. The original SMZ had a weak fluorescence signal in comparison to deionized water (Fig. S10(a) and (b)). The obvious fluorescence signals were generated when SMZ was treated for 60 min (Fig. S10(d)), which demonstrated that some intermediate products were produced. At the same time, the fluorescence signals became strong with the increase in reaction time, indicating that more intermediates were generated. By LC-MS, some intermediates were identified and the m/z were 284, 270, 268, 255, 175, 174, 118, 115, 109, 108, 101, and 99, respectively. According to the confirmed intermediates, the possible SMZ degradation pathways were proposed, as displayed in Fig. 10. There were three possible transformation pathways for SMZ degradation. Path I: the bond of sulfanilamide of SMZ molecule ($m/z = 254$) was broken and the products with $m/z = 108$ and 99 were generated. A product with $m/z = 101$ was produced by reactions opening a ring. Path II: SMZ was oxidized by •OH and the product of $m/z = 270$ was generated. The bond of sulfanilamide was broken and the product of $m/z = 115$ was generated. A product with $m/z = 118$ was also produced by reactions opening a ring. Path III: the amino of SMZ was gradually oxidized and the products with nitroso ($m/z = 268$) and nitro ($m/z = 284$) were generated. Then, a product of hydroxylation ($m/z = 255$) was obtained by oxidation. Subsequently, the bond of sulfanilamide was broken and a product with $m/z = 174$ was got. This was followed by the production of the products with $m/z = 175$ and 109 by oxidation. Lastly, the intermediate products were completely decomposed by ring opening reactions to achieve the mineralization of SMZ, and inorganic products such as H_2O, CO_2, SO_4^{2-}, NO_3^- were generated. The mineralization products (SO_4^{2-} and NO_3^-) were also detected by Ion Chromatography. And the concentration of SO_4^{2-} and NO_3^- were 0.34 and 2.30 mg L^{-1} at 120 min, respectively. This result further confirmed the decomposition of SMZ. The results of LC-MS showed that nitro aromatic compound ($C_{10}H_{10}N_3O_5S^+$) and nitroso aromatic compound ($C_{10}H_{10}N_3O_4S^+$) were generated during the degradation process of SMZ. While nitro aromatic compounds or/and nitroso aromatic compounds are significant toxicity to human. Their mutagenicity, recalcitrance, and tendency to accumulate in the environment make them considered as priority pollutants by the United States Environmental Protection Agency and many other countries [52–54]. Gilbert and Sale [55] also posed that the accumulation of intermediate products (Nitro aromatic compounds) of energetic compounds that pose concerns. In addition, the toxicity of the intermediate by-products was evaluated via the toxicity Estimation Software tool (T.E.S.T., 5.1.1.0) [20]. Among these intermediates, the bioaccumulation factors of P1, P3, P6, P7 and the mutagenicity of P1 and P6 could not be evaluated. As shown in Fig. S11(a), the bioaccumulation factors of the intermediate by-products obvious decreased except for P9. At the same time, the developmental toxicity of all the intermediates reduced (Fig. S11(b)). However, the intermediates exhibited slight enhancement in mutagenicity in comparison to the original SMZ except for P4 (Fig. S11(c)). Although the intermediate by-products were mutagenicity negative except for P3, and the mutagenicity of the intermediate by-products also should be concerned.

3.4. Practicability of U-C_3N_5/SPC/Visible light system

To investigate the practicability of the U-C_3N_5/SPC/Visible light system, experiments with different light sources (LED light (30 W), sunlight) and various water sources were carried out. As Fig. S12(a)

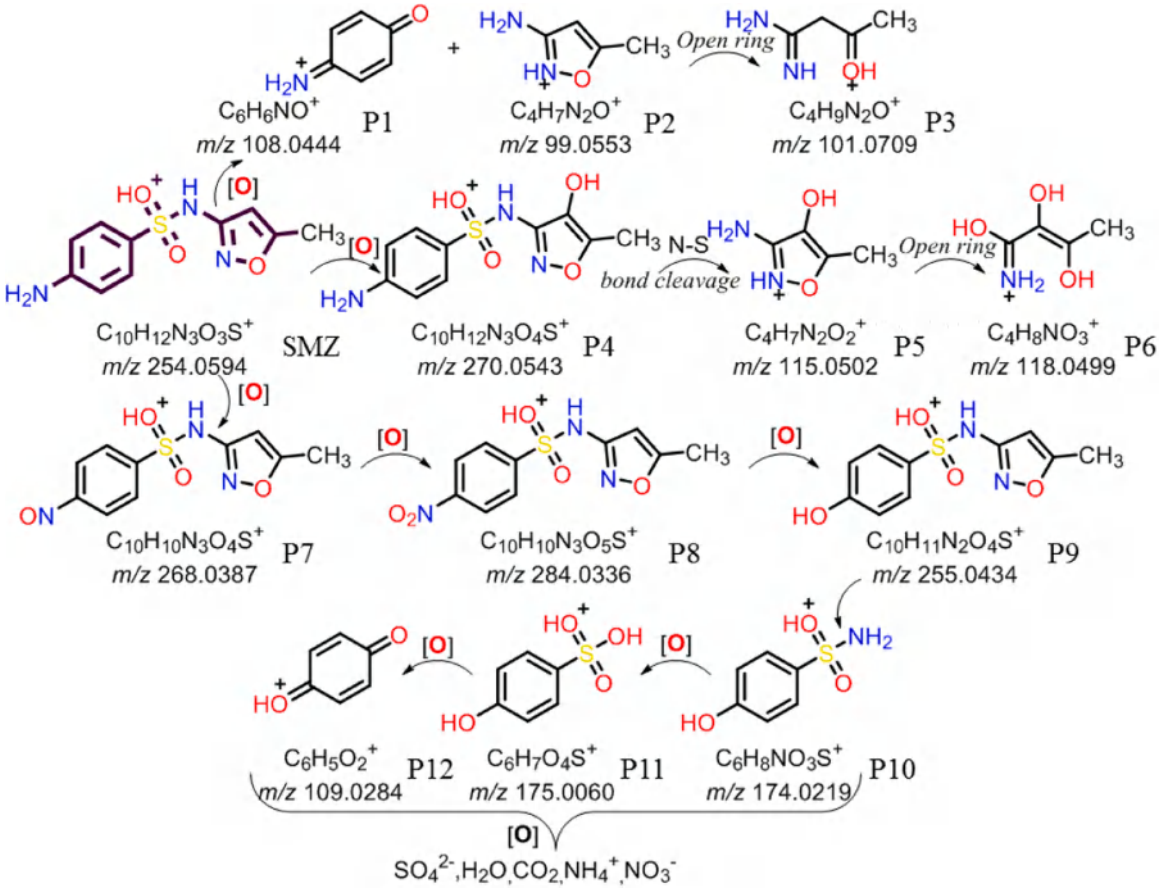

Fig. 10. The proposed degradation pathways of SMZ.

depicted, 32.99% and 9.23% of SMZ were removed in U-C_3N_5/SPC/LED light system and U-C_3N_5/LED light system in 210 min, respectively. The low removal efficiency of SMZ in the U-C_3N_5/SPC/LED light system might be attributed to the low light power intensity of LED light. By contrast, the removal efficiency of SMZ reached 92.78% in U-C_3N_5/SPC/sunlight system (The light power intensity (μW cm^{-2}) at various time was marked in Fig. S12(b)). Simultaneously, 39.58% of SMZ was also removed in the sunlight system alone, which might be due to the existence of UV light in sunlight which can degrade SMZ.

The degradation experiments were implemented with various water sources and the physical-chemical parameters of various water matrices were supplied in Table S10. As Fig. S12(c) exhibited, the degradation efficiency of SMZ followed the order: Xiangjiang River water > Effluent > Tap water > Chuansipo Lake water > Deionized water. The relative low removal efficiency of SMZ in deionized water might be due to the following two reasons. The first one was that the pH value of deionized water was lower than that of other water matrices. According to the result of the influence of pH values, low pH led to a low degradation efficiency of SMZ. The other one was that there existed trace organic matter in other water source except for deionized water. And it was reported that the concentration of •OH and/or $•O_2^-$ could be increased due to trace organic matter exciting by light [56,57]. Except for SMZ, other contaminants were also degraded by U-C_3N_5/SPC/Visible light system. As Fig. S12(d) revealed, CIP and TC-HCl were easy to remove. 100% of TC-HCl and 87.19% of CIP were removed in 120 min, respectively. Whereas, the degradation efficiency of 2,4-DCP, BPA and NPX was low. The different degradation efficiency of various pollutants might be due to the selectivity of active species to pollutants [58].

As we all know, powder materials are not convenient for solid-liquid separation during the process of usage. And additional costs are generated during the practical application. To overcome this defect, a U-C_3N_5/gelatin aerogel (U-C_3N_5/GA) composite was obtained. The ability of U-C_3N_5/GA to activate SPC was explored via the degradation of SMZ with the irradiation of visible light (λ > 420 nm) and sunlight (Nov. 26, 2021, 09:17–12:47). The effluent was used as the medium. As Fig. 11 shown, GA could not activate SPC with the irradiation of visible light and sunlight, and SMZ was almost not degraded. At the same time, the removal rate was low with the irradiation of sunlight, which might due to the scattering of UV light. By contrast, up to 96.37% of SMZ was removed in U-C_3N_5/GA+SPC system with the irradiation of visible light or sunlight in 210 min. This result implied that U-C_3N_5/GA could activate SPC. Moreover, U-C_3N_5/GA was easily separated from the system without energy-consuming. Thus, U-C_3N_5/GA had excellent practicability to activate SPC for SMZ degradation.

4. Conclusion

In this work, metal-free U-C_3N_5 for SPC activation under visible light irradiation was investigated. The performance of U-C_3N_5 was better than that of C_3N_5, U-C_3N_4 and C_3N_4 due to its excellent carrier separation ability. After treatment, a 93.97% of SMZ was removed in 120 min by 0.4 g L^{-1} U-C_3N_5 and 0.1 g L^{-1} SPC under visible light irradiation. The •OH, $•O_2^-$, $^1O_2$, $•CO_3^-$ and h^+ were all involved in SMZ degradation. The U-C_3N_5/SPC/Visible light system exhibited excellent degradation efficiency of SMZ with various influence factors (anions, pH, dissolved organic matter, water matrices, and so on). At the same time, the U-C_3N_5/SPC/sunlight system also displayed acceptable removal efficiency of SMZ. Additionally, the U-C_3N_5 displayed favorable stability. The cytotoxicity of SMZ was reduced after treatment. Lastly, a U-C_3N_5/GA composite was obtained to facilitate the recycling of U-C_3N_5. In short, the combination of metal-free photocatalysis with SPC has been demonstrated to efficiently degrade sulfonamide antibiotics.

CRediT authorship contribution statement

Chi Ma: Experimental measurement, Data curation, Writing-Original draft preparation. **Zhigang Yu:** Methodology, Manuscript revise. **Jingjing Wei:** Manuscript revise. **Chang Tan:** Manuscript revise. **Xu Yang:** Manuscript revise. **Tantan Wang:** Manuscript revise. **Guanlong Yu:** Manuscript revise. **Chang Zhang:** Conceptualization, Methodology, Funding acquisition, Manuscript revise. **Xin Li:** Conceptualization, Methodology, Manuscript revise.

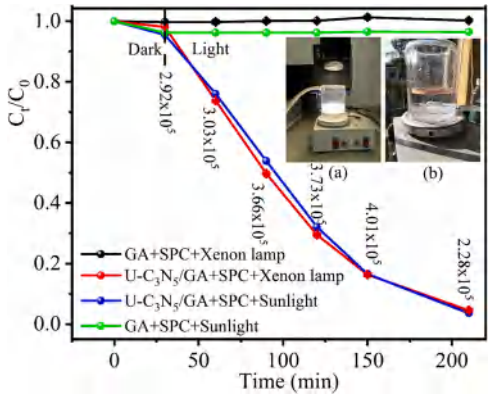

Fig. 11. Degradation of SMZ in U-C_3N_5/GA+SPC+visible light or sunlight system. (a) photograph with the Xenon lamp irradiation, (b) photograph with the sunlight irradiation. Experimental conditions: $C_{SMZ,\ initial}$= 10 mg L^{-1}, $C_{photocatalyst}$= 2000 mg L^{-1}, C_{SPC}= 100 mg L^{-1}, T = 25 ± 0.5 °C.

Declaration of Competing Interest

The authors declare the following financial interests/personal relationships which may be considered as potential competing interests Chang Zhang reports financial support was provided by National Natural Science Foundation of China.

Acknowledgments

This research was supported by the National Natural Science Foundation of China [grant numbers 51879102].

Appendix A. Supporting information

Supplementary data associated with this article can be found in the online version at doi:10.1016/j.apcatb.2022.121951.

References

[1] X.Y. Lou, Z.Y. Liu, C.L. Fang, Y.Y. Tang, J. Guan, Y.G. Guo, X. Zhang, Y.F. Shi, D. M. Huang, Y.Q. Cai, Fate of sulfamethoxazole and potential formation of haloacetic acids during chlorine disinfection process in aquaculture water, Environ. Res. 204 (2022), 111958, https://doi.org/10.1016/j.envres.2021.111958.
[2] Z.H. Pan, Y.J. Zhu, L.Y. Li, Y.N. Shao, Y.H. Wang, K.F. Yu, H.X. Zhu, Y.Y. Zhang, Transformation of norfloxacin during the chlorination of marine culture water in the presence of iodide ions, Environ. Pollut. 246 (2019) 717–727, https://doi.org/10.1016/j.envpol.2018.12.058.
[3] J. Du, H.X. Zhao, S.S. Liu, H.J. Xie, Y. Wang, J.W. Chen, Antibiotics in the coastal water of the South Yellow Sea in China: occurrence, distribution and ecological risks, Sci. Total Environ. 595 (2017) 521–527, https://doi.org/10.1016/j.scitotenv.2017.03.281.
[4] Y.H. Zhong, Z.F. Chen, X.X. Dai, S.S. Liu, G.M. Zheng, X.P. Zhu, S.G. Liu, Y. Yin, G. G. Liu, Z.W. Cai, Investigation of the interaction between the fate of antibiotics in aquafarms and their level in the environment, J. Environ. Manag. 207 (2018) 219–229, https://doi.org/10.1016/j.jenvman.2017.11.030.
[5] M. Mohammadzadeh, M. Montaseri, S. Hosseinzadeh, M. Majlesi, E. Berizi, M. Zare, Z. Derakhshan, M. Ferrante, G.O. Conti, Antibiotic residues in poultry tissues in Iran: a systematic review and meta-analysis, Environ. Res. 204 (2022), 112038, https://doi.org/10.1016/j.envres.2021.112038.
[6] X.M. Liu, D. Wang, L. Wang, J.C. Tang, Dissolved biochar eliminates the effect of Cu(II) on the transfer of antibiotic resistance genes between bacteria, J. Hazard. Mater. 424 (2022), 127251, https://doi.org/10.1016/j.jhazmat.2021.127251.
[7] L. Li, R.N. Guo, S. Zhang, Y.M. Yuan, Sustainable and effective degradation of aniline by sodium percarbonate activated with UV in aqueous solution: Kinetics,

mechanism and identification of reactive species, Environ. Res. (2021), 112176, https://doi.org/10.1016/j.envres.2021.112176.
[8] S.M. Arnold, W.J. Hickey, R.F. Harris, Degradation of atrazine by fenton's reagent: condition optimization and product quantification, Environ. Sci. Technol. 29 (8) (1995) 2083–2089, https://doi.org/10.1021/es00008a030.
[9] H. Wang, L. Zhang, C. Hu, X. Wang, L. Lyu, G. Sheng, Enhanced degradation of organic pollutants over Cu-doped $LaAlO_3$ perovskite through heterogeneous Fenton-like reactions, Chem. Eng. J. 332 (2018) 572–581, https://doi.org/10.1016/j.cej.2017.09.058.
[10] C.T. Benatti, C.R.G. Tavares, E. Lenzi, Sulfate removal from waste chemicals by precipitation, J. Environ. Manag. 90 (1) (2009) 504–511, https://doi.org/10.1016/j.jenvman.2007.12.006.
[11] P.Z. Yang, Y.F. Ji, J.H. Lu, Transformation of ammonium to nitrophenolic byproducts by sulfate radical oxidation, Water Res 202 (2021), 117432, https://doi.org/10.1016/j.watres.2021.117432.
[12] J.Z. Wang, C.S. Cao, Y. Zhang, Y.Q. Zhang, L.Y. Zhu, Underneath mechanisms into the super effective degradation of PFOA by BiOF nanosheets with tunable oxygen vacancies on exposed (101) facets, Appl. Catal. B Environ. 286 (2021), 119911, https://doi.org/10.1016/j.apcatb.2021.119911.
[13] F.Y. Du, Z. Lai, H.Y. Tang, H.Y. Wang, C.X. Zhao, Construction and application of BiOCl/Cu-doped Bi_2S_3 composites for highly efficient photocatalytic degradation of ciprofloxacin, Chemosphere 287 (2022), 132391, https://doi.org/10.1016/j.chemosphere.2021.132391.
[14] Z.R. Miao, Q.L. Wang, Y.F. Zhang, L.P. Meng, X.X. Wang, In situ construction of S-scheme AgBr/BiOBr heterojunction with surface oxygen vacancy for boosting photocatalytic CO_2 reduction with H_2O, Appl. Catal. B Environ. 301 (2022), 120802, https://doi.org/10.1016/j.apcatb.2021.120802.
[15] Y. Zhang, A.R. Sun, M.Y. Xiong, D.K. Macharia, J.S. Liu, Z.G. Chen, Ma.Q. Li, L. S. Zhang, TiO_2/BiOI p-n junction-decorated carbon fibers as weavable photocatalyst with UV–vis photoresponsive for efficiently degrading various pollutants, Chem. Eng. J. 415 (2021), 129019, https://doi.org/10.1016/j.cej.2021.129019.
[16] K. Sekar, C. Chuaicham, B. Vellaichamy, W. Li, W. Zhuang, X.H. Lu, B. Ohtani, K. Sasaki, Cubic Cu_2O nanoparticles decorated on TiO_2 nanofiber heterostructure as an excellent synergistic photocatalyst for H_2 production and sulfamethoxazole degradation, Appl. Catal. B Environ. 294 (2021), 120221, https://doi.org/10.1016/j.apcatb.2021.120221.
[17] G.F. Liao, Y. Gong, L. Zhang, H.Y. Gao, G.J. Yang, B.Z. Fang, Semiconductor polymeric graphitic carbon nitride photocatalysts: the "holy grail" for the photocatalytic hydrogen evolution reaction under visible light, Energy Environ. Sci. 12 (7) (2019) 2080–2147, https://doi.org/10.1039/C9EE00717B.
[18] C. Ma, J.J. Wei, K.N. Jiang, Z.Z. Yang, X. Yang, K.H. Yang, Y. Zhang, C. Zhang, Self-assembled micro-flowers of ultrathin Au/BiOCOOH nanosheets photocatalytic degradation of tetracycline hydrochloride and reduction of CO_2, Chemosphere 283 (2021) 131228–131237, https://doi.org/10.1016/j.chemosphere.2021.131228.
[19] L.C. Yue, J. Cheng, J.J. Hua, H.Q. Dong, J.H. Zhou, A sodium percarbonate/ultraviolet system generated free radicals for degrading capsaicin to alleviate inhibition of methane production during anaerobic digestion of lipids and food waste, Sci. Total Environ. 761 (2021), 143269, https://doi.org/10.1016/j.scitotenv.2020.143269.
[20] Y.J. Li, H.R. Dong, L. Li, J.Y. Xiao, S.J. Xiao, Z.L. Jin, Efficient degradation of sulfamethazine via activation of percarbonate by chalcopyrite, Water Res 202 (2021), 117451, https://doi.org/10.1016/j.watres.2021.117451.
[21] D.Y. Li, Y. Xiao, M.J. Pu, J. Zan, S.Y. Zuo, H.M. Xu, D.S. Xia, A metal-free protonated g-C_3N_4 as an effective sodium percarbonate activator at ambient pH conditions: Efficiency, stability and mechanism, Mater. Chem. Phys. 231 (2019) 225–232, https://doi.org/10.1016/j.matchemphys.2019.04.016.
[22] C.M. Li, H.H. Wu, D.Q. Zhu, T.X. Zhou, M. Yan, G. Chen, J.X. Sun, G. Dai, F. Ge, H. J. Dong, High-efficient charge separation driven directionally by pyridine rings grafted on carbon nitride edge for boosting photocatalytic hydrogen evolution, Appl. Catal. B Environ. 297 (2021), 120433, https://doi.org/10.1016/j.apcatb.2021.120433.
[23] H.J. Dong, Y. Zuo, N. Song, S.H. Hong, M.Y. Xiao, D.Q. Zhu, J.X. Sun, G. Chen, C. M. Li, Bimetallic synergetic regulating effect on electronic structure in cobalt/vanadium co-doped carbon nitride for boosting photocatalytic performance, Appl. Catal. B Environ. 287 (2021), 119954, https://doi.org/10.1016/j.apcatb.2021.119954.
[24] J.L. Zhang, B.H. Jing, Z.Y. Tang, Z.M. Ao, D.H. Xia, M.S. Zhu, S.B. Wang, Experimental and DFT insights into the visible-light driving metal-free C_3N_5 activated persulfate system for efficient water purification, Appl. Catal. B Environ. 289 (2021), 120023, https://doi.org/10.1016/j.apcatb.2021.120023.
[25] S.Y. Qi, Y.C. Fan, J.R. Wang, X.H. Song, W.F. Li, M.W. Zhao, Metal-free highly efficient photocatalysts for overall water splitting: C_3N_5 multilayers, Nanoscale 12 (2020) 306, https://doi.org/10.1039/c9nr08416a.
[26] S. Vadivela, S. Hariganesh, Bappi Paul, Saravanan Rajendran, Aziz Habibi-Yangjeh, D. Maruthamania, M. Kumaravel, Synthesis of novel AgCl loaded g-C_3N_5 with ultrahigh activity as visible light photocatalyst for pollutants degradation, Chem. Phys. Lett. 738 (2020), 136862, https://doi.org/10.1016/j.cplett.2019.136862.
[27] H.Y. Wang, M.X. Li, Q.J. Lu, Y.M. Cen, Y.Y. Zhang, S.Z. Yao, A. Mesoporous Rod-like, g-C_3N_5 synthesized by salt-guided strategy: as a superior photocatalyst for degradation of organic pollutant, ACS Sustain. Chem. Eng. 7 (2019) 625–631, https://doi.org/10.1021/acssuschemeng.8b04182.
[28] H.F. Yin, Y. Cao, T.L. Fan, M. Zhang, J.C. Yao, P.F. Li, S.M. Chen, X.H. Liu, In situ synthesis of Ag_3PO_4/C_3N_5 Z-scheme heterojunctions with enhanced visible-light-responsive photocatalytic performance for antibiotics removal, Sci. Total Environ. 754 (2021), 141926, https://doi.org/10.1016/j.scitotenv.2020.141926.
[29] T.Y. Liu, G.J. Yang, W. Wang, C.X. Wang, M. Wang, X.N. Sun, P. Xu, J.T. Zhang, Preparation of C_3N_5 nanosheets with enhanced performance in photocatalytic methylene blue (MB) degradation and H_2-evolution from water splitting, Environ. Res. 188 (2020), 109741, https://doi.org/10.1016/j.envres.2020.109741.
[30] S.B. Yang, Y.J. Gong, J.S. Zhang, L. Zhan, L.L. Ma, Z.Y. Fang, R. Vajtai, X.C. Wang, P.M. Ajayan, Exfoliated graphitic carbon nitride nanosheets as efficient catalysts for hydrogen evolution under visible light, Adv. Mater. 25 (2013) 2452–2456, https://doi.org/10.1002/adma.201204453.
[31] P. Kumar, E. Vahidzadeh, U.K. Thakur, P. Kar, K.M. Alam, A. Goswami, N. Mahdi, K. Cui, G.M. Bernard, V.K. Michaelis, K. Shankar, C_3N_5: a low bandgap semiconductor containing an azo-linked carbon nitride framework for photocatalytic, photovoltaic and adsorbent applications, J. Am. Chem. Soc. 141 (2019) 5415–5436, https://doi.org/10.1021/jacs.9b00144.
[32] D.H. Park, K.S. Lakhi, K. Ramadass, M.K. Kim, S.N. Talapaneni, S. Joseph, U. Ravon, K. Al-Bahily, A. Vinu, Energy efficient synthesis of ordered mesoporous carbon nitrides with a high nitrogen content and enhanced CO_2 capture capacity, Chem. Eur. J. 23 (2017) 10753–10757, https://doi.org/10.1002/chem.201702566.
[33] S.N. Talapaneni, G.P. Mane, D.-H. Park, K.S. Lakhi, K. Ramadass, S. Joseph, W. M. Skinner, U. Ravon, K. Al-Bahily, A. Vinu, Diaminotetrazine based mesoporous C_3N_6 with a well-ordered 3D cubic structure and its excellent photocatalytic performance for hydrogen evolution, J. Mater. Chem. A 5 (2017) 18183–18192, https://doi.org/10.1039/C7TA04041E.
[34] X. Li, J. Zhang, L. Shen, Y. Ma, W. Lei, Q. Cui, G. Zou, Preparation and characterization of graphitic carbon nitride through pyrolysis of melamine, Appl. Phys. A Mater. Sci. Process 94 (2009) 387–392, https://doi.org/10.1007/s00339-008-4816-4.
[35] J.L. Zhang, Z. Ma, Ag-Ag_3VO_4/$AgIO_3$ composites with enhanced visible-light driven catalytic activity, J. Colloid Interfaces Sci. 524 (2018) 16–24, https://doi.org/10.1016/j.jcis.2018.04.001.
[36] G.G. Zhang, M.W. Zhang, X.X. Ye, X.Q. Qiu, S. Lin, X.C. Wang, Iodine modified carbon nitride semiconductors as visible light photocatalysts for hydrogen evolution, Adv. Mater. 26 (2014) 805–809, https://doi.org/10.1002/adma.201303611.
[37] Y.Y. Kang, Y.Q. Yang, L.C. Yin, X.D. Kang, L.Z. Wang, G. Liu, H.M. Cheng, Selective breaking of hydrogen bonds of layered carbon nitride for visible light photocatalysis, Adv. Mater. 28 (2016) 6471–6477, https://doi.org/10.1002/adma.201601567.
[38] L. Shang, B. Tong, H.J. Yu, G.I.N. Waterhouse, C. Zhou, Y.F. Zhao, M. Tahir, L. Z. Wu, C.H. Tung, T.R. Zhang, CdS nanoparticle-decorated Cd nanosheets for efficient visible light-driven photocatalytic hydrogen evolution, Adv. Energy Mater. 6 (2016) 1501241, https://doi.org/10.1002/aenm.201501241.
[39] L. Wang, P.X. Jin, S.H. Duan, J.W. Huang, H.D. She, Q.Z. Wang, T.C. An, Accelerated fenton-like kinetics by visible-light-driven catalysis over iron(III) porphyrin functionalized zirconium MOF: effective promotion on the degradation of organic contaminants, Sci. Bull. 64 (2019) 926–933, https://doi.org/10.1016/j.scib.2019.05.012.
[40] Z.F. Yu, L.Y. Wang, X.J. Mu, C.C. Chen, Y.Y. Wu, J. Cao, Y. Tang, Intramolecular electric field construction in metal phthalocyanine as dopant-free hole transporting material for stable perovskite solar cells with >21% efficiency, Angew. Chem. Int. Ed. 60 (2021) 6294–6299, https://doi.org/10.1002/anie.202016087.
[41] Z.H. Fang, L.Y. Wang, X.J. Mu, B. Chen, Q. Xiong, W.D. Wang, J.X. Ding, P. Gao, Y. Y. Wu, J. Cao, Grain boundary engineering with self-assembled porphyrin supramolecules for highly efficient large-area perovskite photovoltaics, J. Am. Chem. Soc. 143 (2021) 18989–18996, https://doi.org/10.1021/jacs.1c07518.
[42] M.Y. Ghaly, H. Georg, M. Roland, H. Roland, Photochemical oxidation of p-chlorophenol by UV/H_2O_2 and photo-Fenton process. A comparative study, Waste Manag. 21 (1) (2001) 41–47, https://doi.org/10.1016/S0956-053X(00)00070-2.
[43] U. Farooq, J. Zhuang, X. Wang, S. Lyu, A recyclable polydopamine-functionalized reduced graphene oxide/Fe nanocomposite (PDA@Fe/rGO) for the enhanced degradation of 1,1,1-trichloroethane, Chem. Eng. J. 403 (2021), 126405, https://doi.org/10.1016/j.cej.2020.126405.
[44] N.K. Daud, B.H. Hameed, Decolorization of acid red 1 by Fenton-like process using rice husk ash-based catalyst, J. Hazard. Mater. 176 (2010) 938–944, https://doi.org/10.1016/j.jhazmat.2009.11.130.
[45] L.J. Xu, J.L. Wang, Fenton-like degradation of 2,4-dichlorophenol using Fe_3O_4 magnetic nanoparticles, Appl. Catal. B Environ. 123 124 (2012) 117–126, https://doi.org/10.1016/j.apcatb.2012.04.028.
[46] L. Li, J. Huang, X.B. Hu, S. Zhang, Q. Dai, H.X. Chai, L. Gu, Activation of sodium percarbonate by vanadium for the degradation of aniline in water: Mechanism and identification of reactive species, Chemosphere 215 (2019) 647–656, https://doi.org/10.1016/j.chemosphere.2018.10.047.
[47] J.A.I. Pimentel, C.D. Dong, S.G. Segura, R.R.M. Abarca, C.W. Chen, M. Daniel, D. Lun, Degradation of tetracycline antibiotics by Fe^{2+}-catalyzed percarbonate oxidation, Sci. Total Environ. 781 (2021), 146411, https://doi.org/10.1016/j.scitotenv.2021.146411.
[48] R.G. Zeep, J. Holgne, H. Bader, Nitrate-induced photooxidation of trace organic chemicals in water, Environ. Sci. Technol. 21 (5) (1987) 443–450, https://doi.org/10.1021/es00159a004.
[49] Y.L. Xiao, X. Liu, Y. Huang, W. Kang, Z. Wang, H. Zheng, Roles of hydroxyl and carbonate radicals in bisphenol a degradation via a nanoscale zero-valent iron/percarbonate system: influencing factors and mechanisms, RSC Adv. 11 (2021) 3636–3644, https://doi.org/10.1039/d0ra08395j.
[50] X.R. Fu, X.G. Gu, S.G. Lu, Z.W. Miao, M.H. Xu, X. Zhang, Z.F. Qiu, Q. Sui, Benzene depletion by Fe^{2+}-catalyzed sodium percarbonate in aqueous Solution, Chem. Eng. J. 267 (2015) 25–33, https://doi.org/10.1016/j.cej.2014.12.104.

[51] S. Sajjadi, A. Khataee, R.D.C. Soltani, N. Bagheri, A. Karimi, A.E.F. Azar, Implementation of magnetic Fe_3O_4@ZIF-8 nanocomposite to activate sodium percarbonate for highly effective degradation of organic compound in aqueous solution, J. Ind. Eng. Chem. 68 (2018) 406–415, https://doi.org/10.1016/j.jiec.2018.08.016.

[52] Y. Mu, R.A. Rozendal, K. Rabaey, J. Keller, Nitrobenzene removal in bioelectrochemical systems, Environ. Sci. Technol. 43 (22) (2009) 8690–8695, https://doi.org/10.1021/es9020266.

[53] P. Jiang, J.T. Zhou, A.L. Zhang, Y.J. Zhong, Electrochemical degradation of p-nitrophenol with different processes, J. Environ. Sci. 22 (4) (2010) 500–506, https://doi.org/10.1016/S1001-0742(09)60140-6.

[54] L. Chen, X. Chen, Y. Bai, Z.N. Zhao, Y.F. Cao, L.K. Liu, T. Jian, J. Hou, Inhibition of Escherichia coli nitroreductase by the constituents in Syzygium aromaticum, Chin. J. Nat. Med. 20 (7) (2022) 506–517, https://doi.org/10.1016/S1875-5364(22)60163-8.

[55] D.M. Gilbert, T. Sale, Sequential electrolyticoxidation and reduction of aqueous phase energeticcompounds, Environ. Sci. Technol. 39 (2005) 1241–1249, https://doi.org/10.1021/es051452k.

[56] J. Ma, N.J.D. Graham, Degradation of atrazine by manganese-catalyzed ozonation: influence of humic substances, Water Res. 33 (1999) 785–793, https://doi.org/10.1016/S0043-1354(98)00266-8.

[57] A. Georgi, A. Schierz, U. Trommler, C.P. Horwitz, T.J. Collins, F.D. Kopinke, Humic acid modified Fenton reagent for enhancement of the working pH range, Appl. Catal. B Environ. 72 (2007) 26–36, https://doi.org/10.1016/j.apcatb.2006.10.009.

[58] Y. Liu, J. Luo, L. Tang, C. Feng, J. Wang, Y. Deng, H. Liu, J. Yu, H. Feng, J. Wang, Origin of the enhanced reusability and electron transfer of the carbon-coated Mn_3O_4 nanocube for persulfate activation, ACS Catal. 10 (24) (2020) 14857–14870, https://doi.org/10.1021/acscatal.0c04049.